American Mineralogist, Volume 105, pages 1547–1555, 2020

Experimental observations of TiO_2 activity in rutile-undersaturated melts

Michael R. Ackerson[1,2,*] and Bjørn O. Mysen[2]

[1]National Museum of Natural History, Smithsonian Institution, 10th and Constitution Avenue NW, Washington, D.C. 20560, U.S.A.
[2]Geophysical Laboratory, Carnegie Institution for Science, 5251 Broad Branch Road NW, Washington, D.C. 20015-1305, U.S.A.

Abstract

An estimate of TiO_2 activity ($a_{TiO_2}^{melt\text{-}sat}$) is necessary for the application of trace-element thermobarometry of magmatic systems where melts are typically undersaturated with respect to rutile/anatase. Experiments were performed in the system SiO_2-Na_2O-TiO_2 to develop two independent methods of estimating $a_{TiO_2}^{melt\text{-}sat}$—one based on the commonly applied rutile-saturation technique and another utilizing a novel Ti-in-tridymite thermometer. It is demonstrated that the rutile-saturation model can lead to an overestimate of $a_{TiO_2}^{melt\text{-}sat}$ relative to TiO_2 activity calculated using the solubility of Ti in tridymite (SiO_2) coexisting with rutile. Overestimation via the rutile-saturation technique is due to variations in the solubility mechanisms of Ti in the melt phase as a function of Ti content. In natural systems, overestimates of $a_{TiO_2}^{melt\text{-}sat}$ will lead to an underestimation of crystallization temperatures by Ti-based trace-element thermobarometers. Although this study is not directly applicable to natural systems, it lays the groundwork for future research on natural composition magmas to constrain TiO_2 activity in melts.

Keywords: Thermobarometry, experimental petrology, Raman, Ti activity

Introduction

Over the past decade, trace-element thermobarometry has emerged as a powerful tool to determine the thermal and barometric histories of igneous and metamorphic rocks. The thermodynamic basis for trace-element thermobarometry requires constraints on the activities of the chemical species involved in the reactions that define the thermobarometers. For example, the Ti-in-quartz thermobarometer (Thomas et al. 2010) is based on the reaction $TiO_2^{rutile} = TiO_2^{quartz}$. Given an equilibrium constant $K_{eq} \approx a_{TiO_2}^{quartz}/a_{TiO_2}^{rutile}$ (a_x^i is the activity of component x in phase i) and by assuming the low concentration of TiO_2 in quartz is within the Henry's Law region such that $a_{TiO_2}^{quartz} = kX_{TiO_2}^{quartz}$ (where k is a Henry's Law constant and X is the mole fraction of TiO_2 in quartz) and rutile is nearly pure ($a_{TiO_2}^{rutile} \approx 1$), the equilibrium Gibbs free energy expression provides a functional form through which experimental data can be fit to arrive at the experimentally calibrated expression:

$$RT\ln X a_{TiO_2}^{quartz} = -60\,952 + 1.520T - 1741P + RT\ln a_{TiO_2}^{melt\text{-}sat} \quad (1)$$

that relates the amount of Ti in quartz to temperature, pressure, and the $a_{TiO_2}^{melt\text{-}sat}$ (see Wark and Watson 2006; Ferry and Watson 2007; Ghiorso and Gualda 2013; Hofmann et al. 2013 for further discussion).

In expression 1, $a_{TiO_2}^{melt\text{-}sat}$ is TiO_2 activity expressed relative to rutile saturation in the melt as opposed to $a_{TiO_2} = 1$ when the system is pure TiO_2. Practically, this means that in a silicate melt at rutile saturation, adding more titania to the melt will result in the crystallization of an equimolar quantity of rutile within the system while the TiO_2 content of the melt remains constant. So, in the presence of rutile, this melt is saturated in TiO_2 (Ghiorso and Gualda 2013). When rutile and quartz grow in equilibrium, $a_{TiO_2}^{melt\text{-}sat} = 1$. However, most quartz- and zircon-bearing igneous and metamorphic rocks do not contain rutile, in which case the system is undersaturated relative to TiO_2 ($a_{TiO_2}^{melt\text{-}sat} < 1$) and $a_{TiO_2}^{melt\text{-}sat}$ must be estimated by other means.

In rutile-undersaturated systems, $a_{TiO_2}^{melt\text{-}sat}$ needs to be estimated by independent means to apply Ti-based trace-element thermobarometers. Several different methods have been proposed to estimate $a_{TiO_2}^{melt\text{-}sat}$ in rutile-undersaturated systems. These include rutile-saturation modeling that relies on the assumption that there is a linear relationship (Henry's Law behavior) between $a_{TiO_2}^{melt\text{-}sat}$ and the amount of TiO_2 ($X_{TiO_2}^{melt}$) dissolved in the melt (Hayden and Watson 2007; Gaetani et al. 2008; Shane et al. 2008; Kularatne and Audétat 2014), compositions of co-crystallizing cubic and rhombohedral iron-titanium oxides (Wark et al. 2007; Ghiorso and Gualda 2013), MELTS and rhyolite-MELTS calculations (Thomas and Watson 2012; Kularatne and Audétat 2014), or by assuming that $a_{TiO_2}^{melt\text{-}sat}$ is buffered by the presence of titanium-rich mineral phases (e.g., titanite and ilmenite, Wark and Watson 2006; Thomas et al. 2010).

In many cases, utilizing multiple techniques to estimate $a_{TiO_2}^{melt\text{-}sat}$ can result in a range of values for $a_{TiO_2}^{melt\text{-}sat}$ For example, $a_{TiO_2}^{melt\text{-}sat}$ estimates for the Bishop Tuff range from ~0.15 by using MELTS to characterize melt inclusions (Thomas and Watson 2012) to ~0.69 from equilibrium between rhombohedral and cubic iron-titanium oxides (Ghiorso and Gualda 2013). The value from rutile-saturation model estimates falls in the middle (~0.55). At 200 MPa and 100 ppm Ti in quartz, this range of $a_{TiO_2}^{melt\text{-}sat}$ yields temperature estimates between ~608 and 793 °C. This discrepancy highlights the need for novel mechanisms to

* E-mail: ackersonm@si.edu

0003-004X/20/0010–1547$05.00/DOI: https://doi.org/10.2138/am-2020-7391

estimate $a_{TiO_2}^{melt\text{-}sat}$ in natural magmatic systems.

An understanding of possible reasons for the apparent variations in $a_{TiO_2}^{melt\text{-}sat}$ estimates and a mechanism by which to accurately predict $a_{TiO_2}^{melt\text{-}sat}$ is critical to the application of Ti-based trace-element thermobarometers. For example, measuring the Ti content of quartz crystallized experimentally in rhyolite bulk compositions at known T and P and various degrees of rutile-undersaturation could be used as a direct probe of $a_{TiO_2}^{melt\text{-}sat}$ that could be applied directly to natural quartz-glass pairs (e.g., melt inclusions in quartz). This would require an experimental approach that can crystallize quartz large enough to analyze from rhyolitic composition melts. However, experimental limitations have thus far hindered a direct experimental approach. It is extremely difficult to grow either quartz or zircon in Si-rich compositions to sizes large enough to analyze for Ti content. This fact has led researchers performing experimentally calibrated trace-element thermobarometers to employ hydrous fluids as a crystallization media in lieu of silicate melts (Watson and Harrison 2005; Thomas et al. 2010; Huang and Audétat 2012). In all of these experimental systems, there is no silicate melt phase, making it impossible to study composition-activity relations at rutile-undersaturation that can be directly applied to natural magmas.

Because of the limitations of using natural compositions, we employ Na-silicate compositions for this study, which have been used as model compounds for natural Si-rich magmas for decades (Zotov and Keppler 1998; Cody et al. 2005; Roskosz et al. 2006; Mysen 2011). In this compositional field, tridymite and rutile can be crystallized in equilibrium with a silicate melt. Although the results from this system are not directly applicable to natural systems, they lay the groundwork for understanding potential variations in $a_{TiO_2}^{melt\text{-}sat}$ estimates in nature. In this study, we will utilize two methods (a rutile-saturation model and a Ti-in-tridymite solubility calibration) to calculate $a_{TiO_2}^{melt\text{-}sat}$ in rutile-undersaturated synthetic glasses. Together with Raman investigation of the structure of Ti-bearing synthetic glasses we will discuss potential mechanisms by which different techniques can result in disparate estimates of $a_{TiO_2}^{melt\text{-}sat}$ and provide a potential framework for future experiments on natural composition melts to understand the causes of disparate estimates of $a_{TiO_2}^{melt\text{-}sat}$.

Methods

All experiments utilized powdered synthetic glass starting materials. Glasses were synthesized from thoroughly mixed SiO_2, Na_2CO_3, and TiO_2 powders by heating first at ~100 °C/h from 700–900 °C to convert Na_2CO_3 to Na_2O, and then at 150 °C/h to ~50–100 °C above their liquidus. The samples were then held at this temperature for 1 h. The melts were quenched to glass by removing from the furnace and allowing to cool rapidly in air. Quenched glasses were powdered in an agate pestle and mortar under ethanol for ~1 h to achieve a glass powder with a <30 μm average grain size.

Powdered glass starting material was loaded into ~5 mm diameter, 8 mm long platinum crucibles, and placed in a Deltech 1-atm vertical tube furnace at their experimental temperatures for at least 24 h. Experiments were quenched by removing the crucibles from the furnace and lightly placing the bottom of the crucible in a water bath to quench the material to glass at room temperature in less than 15 s. Glasses were removed from the crucibles, after which crucibles were inspected for leaks by filling with ethanol to ensure no water incursion upon quench. Experiments were performed on bulk compositions along $Na_2O{\cdot}8SiO_2$(NS8)-TiO_2 join with 0–20 mol% TiO_2 (Fig. 1). We use the sample nomenclature TiXNS8, where X is the mol% TiO_2 in the bulk composition. The system SiO_2-Na_2O-TiO_2 was chosen for several reasons. First, its chemical simplicity allows for more accurate interpretation of Raman spectra than would be possible in natural multicomponent compositions. This advantage makes it possible to interpret solution mechanisms

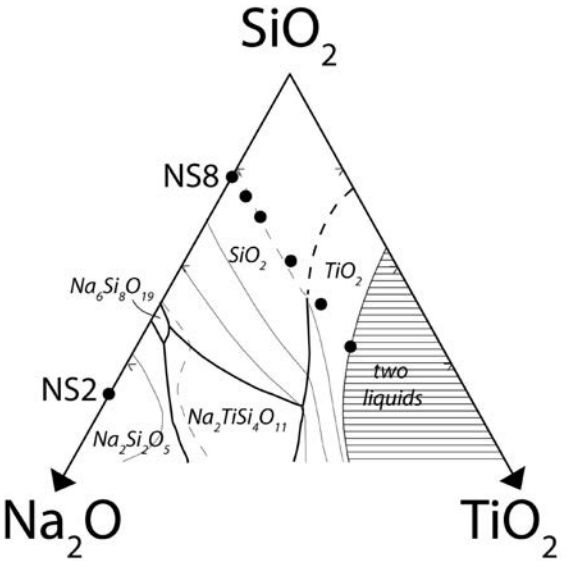

Figure 1. Upper portion of the SiO_2-Na_2O-TiO_2 phase diagram (Glasser and Maar 1979). Experimental bulk compositions are represented by black circles. Gray curves are isotherms along the liquidus surface and solid black lines are liquidus phase boundaries. All experiments except those 20 mol% TiO_2 were within the tridymite liquidus phase field.

that govern Ti incorporation in the melt via Raman spectroscopy. Second, initial experiments performed in haplogranitic bulk compositions were performed at lower temperatures due to quartz-out reactions occurring relatively close to the solidus temperature (Piwinskii 1973; Maaløe and Wyllie 1975; Johannes 1984). As such, quartz crystals in these experiments were too small for accurate electron microprobe analyses (typically <1 μm). In the system SiO_2-Na_2O-TiO_2, tridymite is stable to higher temperatures, which enabled crystals to grow to 25–30 μm on average. This is sufficiently large to perform high-quality chemical analysis of the tridymite grains.

Both starting material and experimental run products were inspected optically and in immersion oils in polarized light to ensure the run products were glasses and to observe crystalline phases below the liquidus. All starting material glasses were transparent with no opalescence, suggesting no cryptocrystalline minerals were present in the synthetic glass starting material. No opalescence was observed in experimental run products either above or below the liquidus. Further X-ray diffraction (XRD) analyses were performed using a Rigaku D-MAX Rapid microdiffractometer with a Mo$K\alpha$ source and image plate detector to validate the mineral phases (e.g., rutile vs. anatase) and to ensure no cryptocrystalline phases had been formed during the experiment or upon quench (Supplementary[1] Fig. S1). Whereas cryptocrystalline anatase has been observed in glasses along the TiO_2-SiO_2 join (e.g., Henderson and Fleet 1995), there is no indication of cryptocrystalline anatase in any of the glasses from this experimental setup along the NS8-TiO_2 join via optical or XRD techniques.

Electron Probe Microanalyzer (EPMA) and scanning electron microscope (SEM) analyses of Ti in tridymite measure consistently similar data (Supplementary[1] Table S1), whereas EPMA data on glasses consistently recorded lower Na content, likely due to Na loss due to the beam current being ~20× greater than the SEM. Because of the reproducibility of Ti in tridymite data between the two techniques and the potential for Na loss in the microprobe analyses, we use SEM data for discussion in this manuscript. It should be noted that even after being held for 24 h at elevated temperature, SEM analyses of the Ti20NS8 glass indicate little to no Na loss from the glass (Supplementary[1] Table S2).

Chemical analyses

Chemical analysis of the mineral and melt run products were conducted on the JEOL 6500F scanning electron microscope (SEM) at the Carnegie Institution of Washington. Quantitative EDS was performed using the Oxford X-Max SDD-EDS detector on the 6500F. EDS spectra were calibrated using a basalt glass standard

following the technique outlined in Armstrong 2014. SEM analyses were performed using a 10 keV ~1 nA beam with 20 s acquisition times. Test analyses of tridymite and glasses were performed on the 8530F EPMA at the Carnegie Institution of Washington to validate the accuracy of the SEM analyses. EPMA analyses were performed using a 10 keV accelerating voltage and 20 nA current for 60 s counting times on tridymite and 30 s on glasses. For both SEM and EPMA analyses the electron beam diameter was defocused to 5 μm on tridymite and 20 μm on the glass to reduce Na loss from the glass. A linear time-dependent intensity correction was enacted for all elements on the microprobe to mitigate the effects of beam damage. EPMA standards were quartz, rutile, and jadeite, for Si, Ti, and Na, respectively. Several tridymite crystals from Ti20NS8 experiments were also extracted from the glass, mounted individually in epoxy and analyzed to verify that secondary fluorescence from the glass did not contribute to measured Ti concentrations in the tridymite. All data presented in the figures are from EDS measurements.

Raman spectroscopy

Raman spectra were collected with a Jasco NRS 3100 confocal Raman spectrometer. The system is equipped with a 490 nm solid-state laser for sample excitation with a laser power of 39.1 mW on the sample. Spectra were collected using a 1200 lines/mm grating, which results in 3 cm^{-1} resolution. Spectra were collected for 40 s over two acquisitions. The spectra were background-corrected with a linear background subtraction from 370 to 1260 cm^{-1}. At higher Ti concentrations, the Raman spectra at low wavenumbers were truncated by the notch filter, making it impractical to attempt curve fitting for this complex region. Furthermore, as the intensity of the low wavenumber peaks increased (region from ~300–500 cm^{-1}), it became impractical to reliably and systematically apply background corrections that would consistently subtract out these regions, as has been done for different Na-silicate glasses that exhibited smaller changes in this low wavenumber region (e.g., Henderson and Fleet 1995). For our purposes, a simple linear background subtraction was deemed the simplest and most effective way to observe changes in the glass structure as a function of bulk TiO_2 content consistently across the sample suite. Above 1260 cm^{-1} spectral intensities were consistent between experiments, indicating that subtraction of backgrounds down to the notch filter is not artificially transforming the low wavenumber regions to higher intensities.

Results

The upper temperature limit investigated was governed by the stability field of the phases of interest. For example the Ti20NS8 experiments were performed up to 1325 °C, above which samples were completely melted. Rutile and tridymite occurred as 5–40 μm crystals in the quenched silicate glasses. No experiments below 20 mol% TiO_2 contained rutile, and tridymite was the liquidus phase in all but the Ti20NS8 experiments (Fig. 2). In rutile-undersaturated experiments, melt compositions followed trends expected in the presence of tridymite crystallization—decreasing temperatures favored increasing tridymite crystallization that in turn led to increasing TiO_2 and Na_2O in the melt (Fig. 3, Table 1). TiO_2 concentrations in tridymite ranged from 0.12 to a maximum of 1.75 wt% TiO_2 in the rutile-saturated Ti20NS8 glass at 1300 °C (Table 2). SEM measurements indicate that the Ti content of tridymite crystals increases with increasing temperature.

In Ti-free NS8 glass, Raman spectra contain peaks consistent with vibrational modes of Si tetrahedral networks, including peaks near 1100 cm^{-1}, 800 cm^{-1} and Q^3-Q^3 Si-O vibrational modes below ~650 cm^{-1} (Bell et al. 1968; Sen and Thorpe 1977; McMillan 1984). Ti-bearing glasses have prominent Raman peaks grouped near ~900, 700–800, and below ~650 cm^{-1} (similar to those observed by Henderson and Fleet 1995). At low Ti concentrations (below 10 mol% TiO_2), the peaks near 900 cm^{-1} dominate the Raman spectra, whereas the lower frequency peaks are dominant at higher Ti concentrations. For a given bulk composition, no significant differences were observed between the corrected spectra for super- and sub-liquidus glasses.

The average coordination of Ti in the melt ([4]-, [5]-, or [6]-fold) and the mechanisms by which Ti is incorporated (as a network-forming or network-modifying cation, or as isolated clusters of Ti) can qualitatively be assessed using Raman spectroscopy of the quenched synthetic glasses. Raman spectra of quenched glasses (Fig. 4) show evidence of significant changes to the structure of the Ti-bearing Na-silicate glasses as a function of Ti content. Overall, the total intensity of the Raman

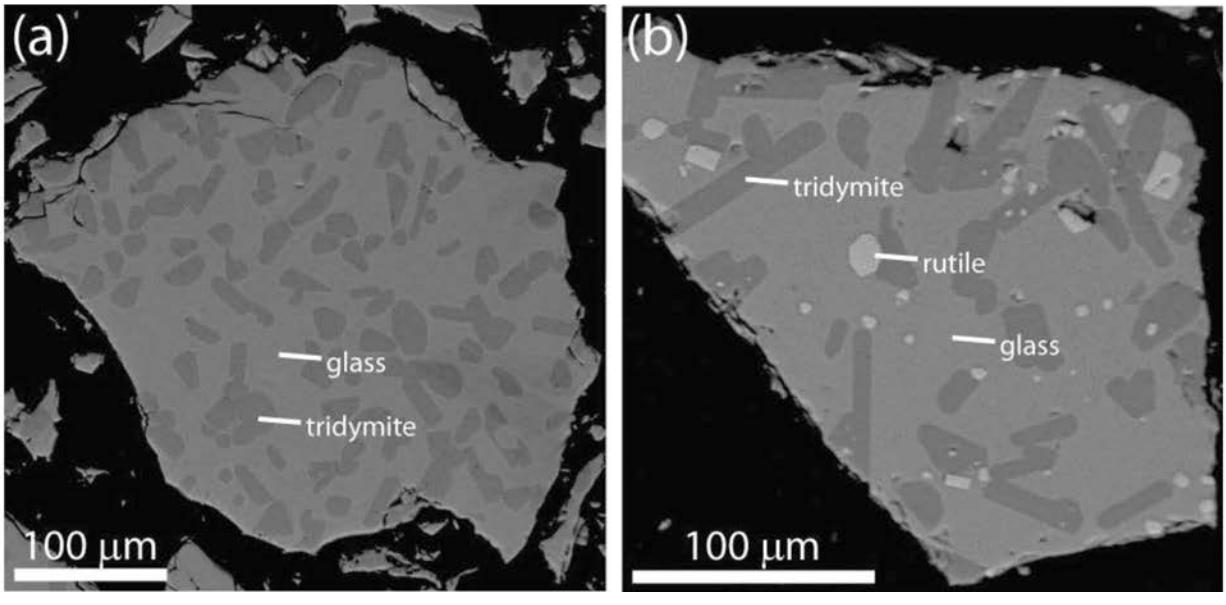

Figure 2. Backscatter-electron images of experimental run products that contain (**a**) tridymite and melt from Ti10NS8 at 1250 °C and (**b**) tridymite, rutile, and melt from Ti20NS8 at 1185 °C.

TABLE 1. Tridymite compositions measured by SEM EDS (wt%)

Bulk TiO_2	T (°C)	SiO_2		TiO_2		Total
		value	SD	value	SD	
2.5	1225	99.06	0.21	0.13	0.05	99.18
2.5	1250	99.20	0.05	0.12	–	99.33
2.5	1275	99.09	0.14	0.12	0.02	99.21
2.5	1300	99.02	0.23	0.13	0.02	99.15
2.5	1325	98.83	0.15	0.13	0.02	98.96
2.5	1325	98.96	0.22	0.13	0.01	99.09
2.5	1350	99.10	0.24	0.13	0.02	99.23
5	1225	98.60	0.97	0.24	0.03	98.84
5	1250	98.98	0.62	0.32	0.19	99.29
5	1275	99.19	0.23	0.26	0.02	99.45
5	1300	98.99	0.24	0.27	0.02	99.26
5	1325	98.59	0.52	0.28	0.03	98.87
5	1350	98.78	0.40	0.27	0.02	99.05
5	1375	98.57	0.28	0.27	0.03	98.84
5	1400	98.13	0.31	0.28	0.01	98.41
5	1425	98.12	0.21	0.28	0.03	98.40
10	1250	98.48	0.84	0.60	0.04	99.08
10	1275	98.79	0.33	0.59	0.03	99.39
10	1300	98.57	0.33	0.62	0.05	99.19
10	1325	98.59	0.35	0.61	0.06	99.20
10	1350	98.66	0.54	0.64	0.02	99.30
10	1375	98.15	0.62	0.65	0.06	98.80
15	1225	97.39	0.19	1.13	0.08	98.51
15	1250	96.18	3.42	1.11	0.06	97.28
15	1275	97.11	1.55	1.12	0.05	98.23
15	1300	97.84	0.33	1.17	0.05	99.01
15	1325	97.70	0.35	1.19	0.06	98.89
15	1350	97.70	0.67	1.21	0.14	98.91
20	960	97.97	0.38	0.72	0.09	98.70
20	1003	98.06	0.52	0.87	0.06	98.93
20	1010	97.82	0.47	0.74	0.16	98.56
20	1053	98.13	0.08	1.00	0.04	99.13
20	1105	92.04	0.52	1.07	0.06	93.11
20	1128	97.77	0.65	1.17	0.09	98.94
20	1145	95.34	7.81	1.12	0.13	96.45
20	1171	96.79	1.92	1.28	0.19	98.08
20	1185	95.25	0.36	1.52	0.08	96.78
20	1200	97.14	0.87	1.45	0.11	98.59
20	1225	97.78	0.21	1.46	0.05	99.24
20	1251	96.60	1.75	1.59	0.13	98.19
20	1277	97.44	0.42	1.74	0.09	99.18
20	1301	97.11	0.40	1.75	0.05	98.86

TABLE 2. Glass compositions measured by SEM EDS (wt%)

Bulk TiO_2	T (°C)	Na_2O		SiO_2		TiO_2		Total
		value	SD	value	SD	value	SD	
2.5	1225	11.83	0.15	81.70	0.15	4.96	0.15	98.49
2.5	1250	12.27	0.38	81.62	0.57	4.91	0.10	98.79
2.5	1275	11.81	0.26	82.64	0.24	4.57	0.11	99.02
2.5	1300	11.85	0.44	82.15	0.52	4.62	0.10	98.62
2.5	1325	11.51	0.52	82.38	0.54	4.17	0.05	98.06
2.5	1325	11.26	0.13	83.56	0.17	4.33	0.08	99.15
2.5	1350	11.13	0.13	84.12	0.15	4.23	0.14	99.48
5	1225	9.81	0.78	78.21	0.20	9.63	0.10	97.65
5	1250	9.66	0.51	78.94	0.29	9.34	0.18	97.93
5	1275	9.48	0.32	79.96	0.13	8.86	0.18	98.29
5	1300	9.24	0.19	80.36	0.37	8.63	0.22	98.23
5	1325	9.10	0.16	80.77	0.31	8.43	0.29	98.30
5	1350	8.72	0.05	81.35	0.41	8.01	0.20	98.09
5	1375	8.43	0.12	82.02	0.24	7.61	0.10	98.05
5	1400	7.68	0.20	82.65	0.49	7.10	0.11	97.44
5	1425	7.38	0.11	83.46	0.25	6.71	0.12	97.56
10	1250	8.11	0.32	72.67	0.12	16.16	0.12	96.94
10	1275	7.91	0.17	72.96	0.28	16.15	0.08	97.03
10	1300	7.80	0.19	74.89	0.18	14.67	0.08	97.36
10	1325	8.10	0.08	74.32	0.10	14.86	0.08	97.28
10	1350	7.03	0.18	76.92	0.31	13.71	0.12	97.66
10	1375	6.09	0.25	76.75	0.16	14.29	0.14	97.14
15	1225	8.29	0.31	65.14	0.23	22.44	0.09	95.87
15	1250	8.11	0.21	66.25	0.14	21.57	0.12	95.92
15	1275	7.66	0.08	67.95	0.14	21.08	0.09	96.69
15	1300	6.93	0.19	69.93	0.18	20.02	0.08	96.88
15	1325	6.42	0.08	71.29	0.10	19.07	0.08	96.78
15	1350	6.87	0.26	72.19	0.24	17.89	0.34	96.95
20	960	2.79	0.12	67.46	0.15	24.51	0.19	94.75
20	1003	2.35	0.63	65.70	0.48	24.64	0.77	92.70
20	1010	2.56	0.12	67.02	0.00	25.12	0.26	94.70
20	1053	9.98	2.31	62.35	0.00	23.95	0.04	96.28
20	1105	5.86	0.66	63.30	0.57	24.79	0.22	93.94
20	1128	5.97	0.55	64.18	0.54	25.45	0.37	95.60
20	1145	9.62	0.58	62.55	0.08	24.33	0.12	96.49
20	1171	9.37	0.17	62.36	0.39	24.71	0.12	96.45
20	1185	9.33	0.10	61.82	0.29	24.61	0.12	95.77
20	1200	8.72	0.31	62.91	0.01	24.84	0.06	96.47
20	1225	9.18	0.32	62.80	0.00	24.67	0.03	96.64
20	1251	8.38	3.07	63.31	0.02	24.97	0.09	96.66
20	1277	7.95	0.87	64.05	0.00	24.78	0.05	96.78
20	1301	7.56	0.89	64.89	0.00	24.12	0.03	96.57

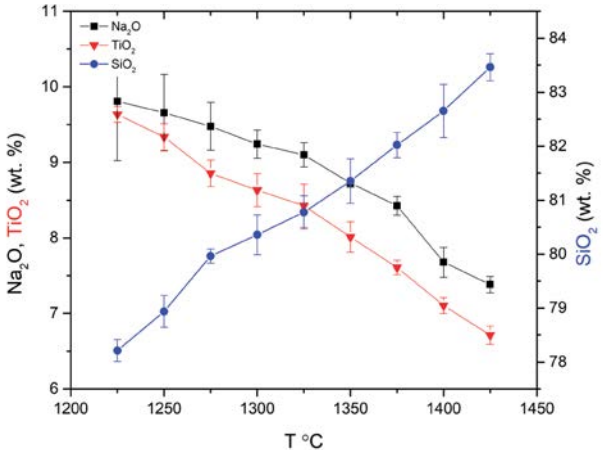

FIGURE 3. Temperature vs. melt composition trends for experiments in the bulk composition Ti5NS8. These rutile-undersaturated experiments show a trend of increasing TiO_2 and Na_2O and decreasing SiO_2 content with decreasing temperature as a result of increased down-temperature crystallization of tridymite (SiO_2). (Color online.)

signal increases with increasing Ti content. The Ti-free NS8 glass contains Raman peaks at ~1100 and ~1150 cm^{-1} that can be attributed to Si-O stretching of Q^3 and Q^4 speciation of Si in the melt, respectively (e.g., Le Losq et al. 2015). Peaks from 300–500 cm^{-1} can be attributed to symmetrical stretching of Si-O-Si bonds (Seifert et al. 1983; Mcmillan et al. 1984) in silicate rings and the peak at ~800 cm^{-1} is attributed to oxygen vibrations (Mysen and Richet 2005).

At low TiO_2 concentrations a set of peaks begins to emerge from ~880–1000 cm^{-1}. These peaks have been attributed to $^{[4]}$Ti as either a network-forming cation or as $^{[5]}$Ti clusters (Henderson and Fleet 1995; Mysen and Neuville 1995). The most intense of these peaks (~900 cm^{-1}) has also been attributed to stretching vibrations of $^{[5]}$Ti (Reynard and Webb 1998) in titanyl groups (Farges 1997). The intensity of this group of peaks continues to increase with increasing Ti content. Peaks that appear prominently between ~650–800 cm^{-1} in the spectra starting around 10 mol% TiO_2 have been attributed to Ti in either $^{[4]}$Ti coordination (similar to Ba_2TiO_4) or $^{[5]}$Ti (similar to fresnoite glass) (Henderson and Fleet 1995). Peaks at low wavenumbers (~300–550 cm^{-1}) also increase in intensity around 10 mol% TiO_2 and continue to increase as Ti content increases. At high Ti concentrations, these peaks eclipse the Si-O-Si peaks

observed in the Ti-free glasses. From the similarities with rutile and anatase spectra, these peaks have been attributed to either [6]Ti as a network modifying cation, or [6]Ti clusters (Mysen and Neuville 1995). Based on these observations from previous work, we have qualitatively separated the Raman spectra into four regions that broadly define the molecular interactions responsible for Raman scattering—"Si" at high wavenumbers, "Ti low" (low average Ti coordination) through "Ti high" (for Ti in [5]- and [6]-fold coordination). These assignments are not meant as strict boundaries, but instead as a means to qualitatively assess changes in the Raman spectra as a function of bulk TiO_2 content of the glasses. An example of these peak components is shown in Supplementary[1] Figure S2.

Discussion

The activity of titanium relative to rutile saturation ($a_{TiO_2}^{melt\text{-}sat}$) will be calculated in two ways. The first approach is a rutile-saturation model that relies on the assumption of a constant activity coefficient, $\gamma_{TiO_2}^{melt\text{-}sat}$, whereas the second approach will utilize a Ti-in-tridymite thermometer calibrated in the present study. The structure and chemistry of the glass as a function of bulk X_{TiO_2} and partitioning between the glass and tridymite can help to elucidate which method most accurately records $a_{TiO_2}^{melt\text{-}sat}$.

Rutile saturation approach

The relationship between activity and composition is generally defined as: $a_{TiO_2}^{melt} = \gamma_{TiO_2}^{melt} \cdot X_{TiO_2}^{melt}$, where $\gamma_{TiO_2}^{melt}$ is the activity coefficient. In an ideal system, $\gamma_{TiO_2}^{melt} = 1$. In natural magmatic compositions where rutile saturates at relatively low $X_{TiO_2}^{melt}$, TiO_2 is assumed to behave within the Henry's Law region such that $\gamma_{TiO_2}^{melt} \approx k$, where k is the Henry's Law constant. In both the ideal and Henry's Law case, there is a linear relationship between $a_{TiO_2}^{melt}$ and $X_{TiO_2}^{melt}$. Therefore, $a_{TiO_2}^{melt}$ can be calculated by dividing the measured value by the rutile-saturated $X_{TiO_2}^{melt}$ (in an ideal case, this value is unity) value:

$$a_{TiO_2}^{ideal} = \frac{1}{X_{TiO_2}^{melt}} \text{ or } a_{TiO_2}^{melt\text{-}sat} = \frac{X_{TiO_2}^{melt}}{X_{TiO_2}^{melt\text{-}sat}}$$

(Hayden and Watson 2007; Hofmann et al. 2013). Here, we will apply a similar rutile saturation technique to our experiments to estimate $a_{TiO_2}^{melt\text{-}sat}$ (hereafter called $a_{TiO_2}^{rut\text{-}sat}$).

To calculate $a_{TiO_2}^{melt\text{-}sat}$ using this technique, we established a rutile saturation surface by measuring $X_{TiO_2}^{melt}$ of rutile-saturated NS8 glasses over a range of temperatures. Over a temperature range of 960–1325 °C, $X_{TiO_2}^{melt}$ varied slightly—from ~0.21 to ~0.20 (Fig. 5). Within the standard deviation of the data, this value is effectively a constant, meaning we can treat the rutile-saturated $X_{TiO_2}^{melt}$ value as a constant ~0.21. We then calculated $a_{TiO_2}^{rut\text{-}sat}$ using this saturation surface and the linear *a-X* assumption by dividing $X_{TiO_2}^{melt}$ measured in the rutile-undersaturated glass by $X_{TiO_2}^{melt}$ in the rutile saturated glass at the same temperature.

Ti-in-tridymite calibration

Rutile-saturated experiments that also contain tridymite were used to calibrate a 1-atm Ti-in-tridymite thermometer (Fig. 6). The Ti content of tridymite in rutile-saturated experiments was fit to an Arrhenius relationship with respect to temperature ($1/T$) by utilizing the same principles as in the Ti-in-quartz calibration at constant pressure (Wark and Watson 2006), which yields the expression:

$$\ln X_{TiO_2}^{tridymite} = -5299.14/T(K) - 0.9242. \quad (2)$$

Similar to Wark and Watson (2006) we assume that the Ti solubility in the tridymite follows Henry's Law behavior such that:

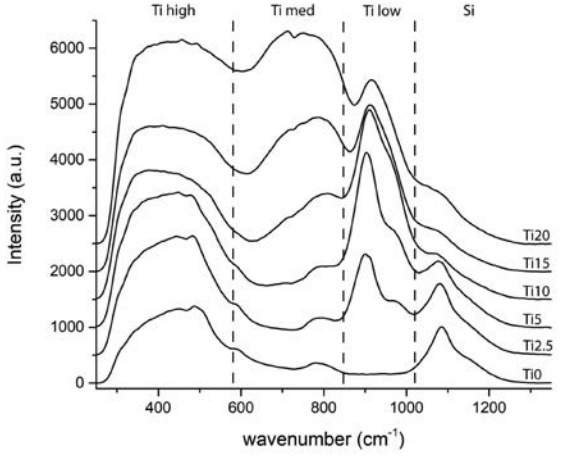

Figure 4. Raman spectra of quenched glasses from selected bulk compositions from Ti-free (NS8) to 20 mol% TiO_2 (Ti20NS8). Changes to the Raman spectra with changes in bulk Ti content can be attributed to changes in the average coordination of Ti in the melt as a function of bulk Ti content. Because peak assignment in these spectra is not straightforward (e.g., Scannell et al. 2016), spectra were grouped into regions whose peaks generally represent Si (Si), lower average coordination Ti ("Ti low"), potentially mixed coordination ("Ti med"), and likely higher average coordination Ti ("Ti high"). Although these regions are broad and intentionally non-specific, the trends indicate a change in Ti coordination in the glass as a function of its bulk TiO_2 content.

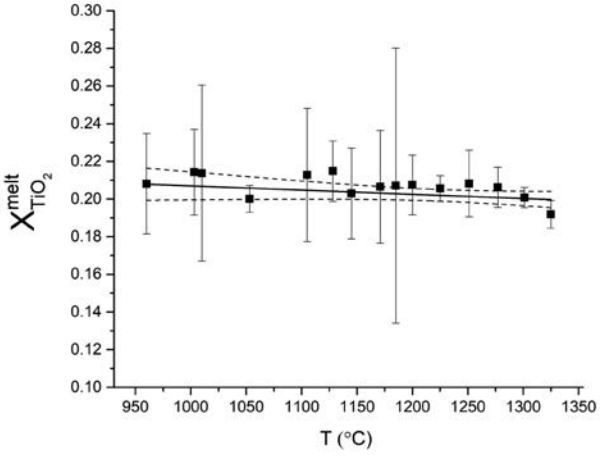

Figure 5. Temperature vs. $X_{TiO_2}^{melt}$ for rutile-saturated Ti20NS8 melts. Error bars are 2σ standard deviation on measurements of $X_{TiO_2}^{melt}$. Over the 341 °C temperature interval, $X_{TiO_2}^{melt}$ varied slightly from 0.2–0.21. $X_{TiO_2}^{melt}$ in rutile-saturated experiments is used to calculate $a_{TiO_2}^{rut\text{-}sat}$.

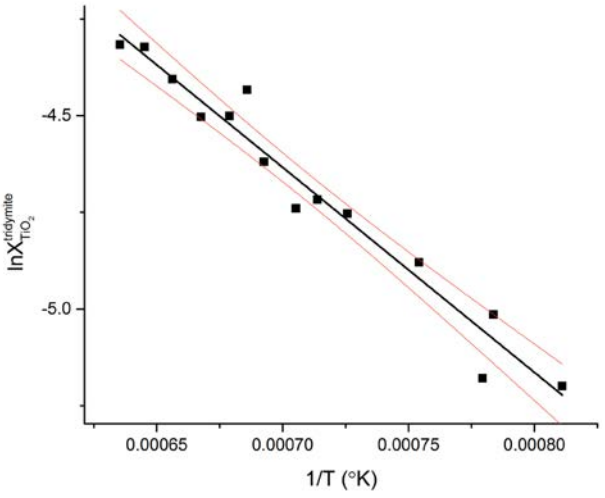

Figure 6. Ti-in-tridymite calibration from rutile-saturated experiments showing the amount of Ti dissolved in tridymite ($\ln X_{TiO_2}^{tridymite}$) as a function of reciprocal temperature. Red curves are the 95% confidence bands on the linear regression. (Color online.)

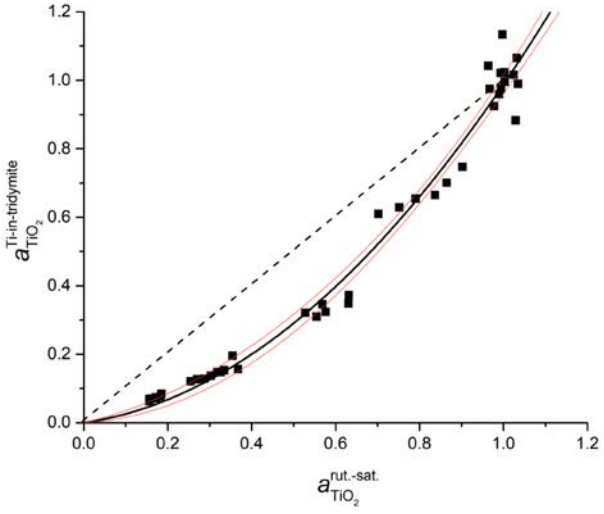

Figure 7. Comparison of $a_{TiO_2}^{Ti\text{-}in\text{-}tridymite}$ and $a_{TiO_2}^{rut\text{-}sat}$ estimates of $a_{TiO_2}^{melt\text{-}sat}$ fitted with a second-order polynomial forced through the origin. Red curves are the 95% confidence bands. Relative to $a_{TiO_2}^{Ti\text{-}in\text{-}tridymite}$, $a_{TiO_2}^{rut\text{-}sat}$ consistently over-predicts $a_{TiO_2}^{melt\text{-}sat}$. (Color online.)

$$a_{TiO_2}^{Ti\text{-}in\text{-}tridymite} = \frac{X_{TiO_2}^{tridymite}}{X_{TiO_2}^{tridymite@sat}} \quad (3)$$

where $X_{TiO_2}^{tridymite@sat}$ is the mole fraction TiO_2 in tridymite at rutile saturation, at a given temperature.

Comparison of $a_{TiO_2}^{melt\text{-}sat}$ estimates

If both methods used to calculate $a_{TiO_2}^{melt\text{-}sat}$ in rutile-undersaturated melts agree, they should co-vary along a line with slope = 1. However, the rutile-saturation activity estimates predict $a_{TiO_2}^{melt\text{-}sat}$ in excess of that from the Ti-in-tridymite estimate (Fig. 7).

Changes in the solubility mechanisms of Ti in the melt as a function of bulk Ti content could result in erroneous estimates of $a_{TiO_2}^{rut\text{-}sat}$ Ti coordination changes can be qualitatively assessed using Raman spectroscopy. Due to the complexity of the Raman spectra and the difficulty of assigning individual peaks to specific features (e.g., Scannell et al. 2016), Raman spectra were binned into discrete regions, labeled "Ti high," "Ti med," "Ti low," and "Si," (Fig. 4). Broadly, increasing the Ti content of the glasses results in changes in Ti coordination and solubility mechanisms in the melt. Although these assignments are intentionally vague, relative changes to the Raman spectra in these regions as a function of bulk TiO_2 correspond to changes in solubility mechanisms for Ti in the melt. These relative changes are the most important factor for observing if Ti solubility mechanisms change in the glasses as a function of bulk TiO_2 content. Several general trends as a function of increasing TiO_2 can be seen in the Raman spectra for superliquidus NS8 glasses. In general, the average coordination of Ti in the melt increases with decreasing wavenumber. This is consistent with other studies of Ti coordination in SiO_2-rich glasses (Chandrasekhar et al. 1980; Henderson and Fleet 1995; Mysen and Neuville 1995; Farges 1997; Reynard and Webb 1998). In lieu of attempting to curve fit the complex Raman spectra, integrating the area under the curves over discrete intervals allows us to interpret changes in the average coordination environment of Ti in the melt as a function of bulk TiO_2 content (Figs. 4 and 8). The Raman spectra have been broken into four regions corresponding to the specific Raman scattering phenomena discussed above. Generally, Ti is incorporated primarily in [4]-fold coordination at low Ti concentrations (Fig. 8). As more Ti is added to the system, the average coordination number of Ti increases. At 20 mol% TiO_2, Ti is primarily incorporated in [5]- and [6]-fold coordination. The important takeaway from the Raman data are that the coordination (and subsequent solubility mechanisms governing Ti incorporation into the melt) changes from almost entirely $^{[4]}$Ti at low concentrations to an average $^{[5]}$Ti or $^{[6]}$Ti higher TiO_2 concentrations.

The Raman spectra demonstrate a distinct change in the character of Ti incorporation in the melt as a function of bulk Ti content. Given that $\gamma_{TiO_2}^{melt}$ is defined relative to the reactions governing the solubility of a species in a melt (e.g., Ryerson 1985), the Raman results suggest that the assumption of constant $\gamma_{TiO_2}^{melt}$ (akin to the Henry's Law assumptions in natural rutile-undersaturated glasses) is invalid for the Ti-NS8 system. Departure from Henry's Law behavior can be seen through partitioning of Ti between tridymite and the melt (Fig. 9). Over a range of temperatures, there is a distinct break in slope of $D_{TiO_2}^{trd/glass}$ at around 5 mol% TiO_2. This break also correlates with the rise of the 900 cm^{-1} peak in the Raman spectra. Henderson et al. (2002) and Scannell et al. (2016) also observed that in Ti-bearing Na-silicate glasses, square pyramidal clusters of [5]-fold Ti start to form around 5 mol% TiO_2. Similar changes in coordination have been observed using Raman in other Ti-bearing Na-silicate glasses (e.g., Scannell et al. 2016). Combined, these observations are a strong indication that the rutile saturation model is over-predicting $a_{TiO_2}^{melt\text{-}sat}$ in our system.

Although Raman spectra likely demonstrate that the rutile

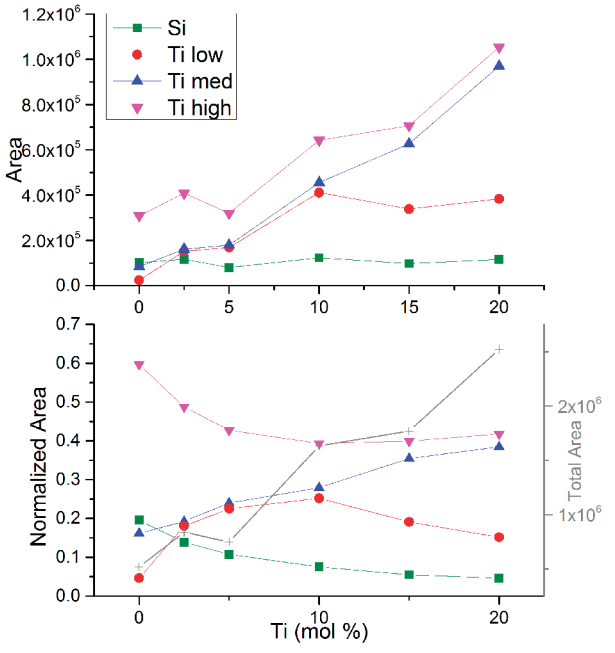

Figure 8. Areas of regions in the Raman spectra (see Fig. 4) that can be attributed to changes in the structure of Ti in the melt as a function of TiO_2. Areas under the background-normalized curves are shown both as the absolute area as well as relative to the total area. As discussed in the text, these regions are intentionally broad and reflect general changes in the structure of the melt. In the case of the "Ti high" region, this is the predominant area in the Ti-free spectrum, and intensity here is due to the symmetrical stretching of Si-O-Si bonds (Seifert et al. 1983; McMillan et al. 1984). As the Ti content of the glasses increased, the intensity of this region increased from peaks related to Ti in higher average coordination (Mysen and Neuville 1995), swamping the Si signal from the Ti-free glass. So, whereas the relative area of this region decreased with increasing Ti (lower panel), the absolute area increased with increasing Ti. The + symbols in the lower panel are the total area under the curve for the Raman spectra, using the right-side y-axis. (Color online.)

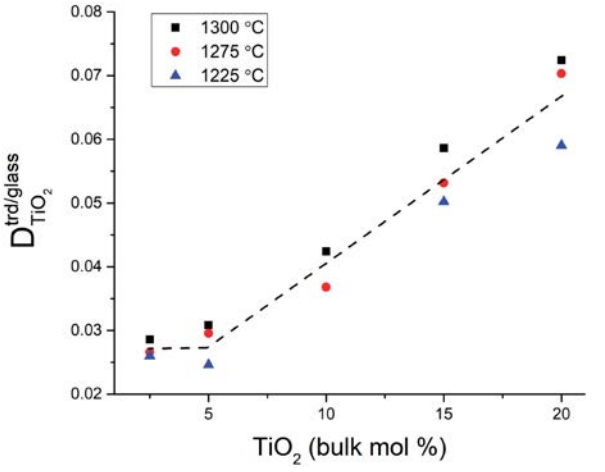

Figure 9. Partitioning of titania between tridymite and quenched glasses. At multiple temperatures, changes in bulk TiO_2 content correlate with changes in the partition coefficient for TiO_2 between tridymite and quenched glass. The major deviation at ~5 mol% TiO_2 corresponds to a change in the coordination behavior of TiO_2 in the melt as seen in Raman spectra of the glasses and likely represents a departure from Henrian behavior of TiO_2 in the glasses. (Color online.)

saturation technique over-predicts $a_{TiO_2}^{melt\text{-}sat}$ it is worth noting that Ti contents in tridymite can be high (up to 1.75 wt% TiO_2). These high concentrations might also be responsible for non-Henrian behavior in the Ti-in-tridymite calibration. For example, at a given bulk TiO_2 content $a_{TiO_2}^{Ti\text{-}in\text{-}tridymite}$ estimates decrease as temperature and the amount of Ti dissolved in tridymite increase (Fig. 7). Even if these systematic deviations are a demonstration of departures from Henry's Law behavior, the magnitude of the deviations is significantly less than those of the rutile saturation model. Further, the Arrhenian behavior of the Ti-in-tridymite calibration (Fig. 6) where Ti concentrations vary from 0.72–1.75 wt% suggests that non-Henrian behavior of Ti in tridymite plays a relatively minor role.

A second-order polynomial fit was applied to the two estimates of $a_{TiO_2}^{melt\text{-}sat}$ (Fig. 7). This fit relates the $a_{TiO_2}^{Ti\text{-}in\text{-}tridymite}$ ($a_{TiO_2}^{melt\text{-}sat}$ calculated through Ti-in-tridymite) estimates to $a_{TiO_2}^{rut\text{-}sat}$ ($a_{TiO_2}^{melt\text{-}sat}$ measured using the rutile-saturation method). Because the Ti-in-tridymite estimates are more likely to predict the actual $a_{TiO_2}^{melt\text{-}sat}$ more accurately, the trend in Figure 7 is a demonstration of the overestimation of $a_{TiO_2}^{melt\text{-}sat}$ using rutile-saturation models relative to $a_{TiO_2}^{Ti\text{-}in\text{-}tridymite}$ methods. This trend can then be used to estimate the effect of a variable $\gamma_{TiO_2}^{melt}$ on thermobarometry that utilizes rutile-saturation models to estimate $a_{TiO_2}^{melt\text{-}sat}$.

Implications for Ti-based trace-element thermobarometry

The high $X_{TiO_2}^{melt}$ required for rutile saturation in the present experiments combined with the chemical simplicity of the NS8 composition make it difficult to assess whether the analogous overestimation of $a_{TiO_2}^{melt\text{-}sat}$ via $a_{TiO_2}^{rut\text{-}sat}$ will be expected in natural silicate melts where rutile saturation occurs at significantly lower $X_{TiO_2}^{melt}$ (Hayden and Watson 2007). The interpretation of the Raman observations indicates that Ti undergoes significant structural changes with variations in $X_{TiO_2}^{melt}$. At low concentrations, Ti appears to be incorporated as $^{[4]}$Ti, whereas Ti is in a higher average coordination state ($^{[5]}$Ti or $^{[6]}$Ti) as rutile saturation in the melt is approached (Fig. 4).

The key reason for the inaccuracy of the rutile saturation estimates in our study is changes in the solubility mechanisms (as inferred by changes in Ti coordination) governing Ti incorporation into the glass. Although direct comparison with natural composition glasses is not practical at this time, similar changes in Ti coordination have been observed in natural composition glasses. For example, Farges and Brown (1997) showed that Ti coordination in rutile-undersaturated glasses shifted from a mixture of [5]-fold and [6]-fold Ti in basaltic melts to a mixture of [4]-fold and [5]-fold in rhyolitic melts.

To correct the overestimation of $a_{TiO_2}^{melt\text{-}sat}$ via the assumption of constant $\gamma_{TiO_2}^{melt}$, we fit a second-order polynomial forced through the origin to the trend between $a_{TiO_2}^{Ti\text{-}in\text{-}tridymite}$ and $a_{TiO_2}^{rut\text{-}sat}$ (Fig. 7):

$$a_{TiO_2}^{Ti\text{-}in\text{-}tridymite} = (0.814 \cdot a_{TiO_2}^{rut\text{-}sat})^2 + 0.174 \cdot a_{TiO_2}^{rut\text{-}sat} \quad (5)$$

which can be applied in correcting $a_{TiO_2}^{rut\text{-}sat}$ estimates of $a_{TiO_2}^{melt\text{-}sat}$ Because Ti solubility mechanisms and changes therein are not precisely known, we fit the data with a second-order polynomial primarily because it was the simplest functional form that best fit the data. Using this fit, if rutile-saturation models predict $a_{TiO_2}^{melt\text{-}sat} = 0.5$, this fit yields a corrected $a_{TiO_2}^{melt\text{-}sat} = 0.29$. In natural systems, this correction for $a_{TiO_2}^{rut\text{-}sat}$ could have a significant influence on petrologic interpretations derived from Ti-based trace-element thermobarometry.

Implications

The results of this study indicate that—in the system SiO_2-TiO_2-Na_2O—rutile-saturation modeling of Ti activity in melts (based on the assumption of a constant $\gamma_{TiO_2}^{melt\text{-}sat}$) can lead to an overestimate of Ti activity in rutile-undersaturated melts. Changes in the incorporation mechanism for Ti in the melt are responsible for changes in the $\gamma_{TiO_2}^{melt\text{-}sat}$ and in turn the overestimation of $a_{TiO_2}^{melt\text{-}sat}$

The findings of this study pertain to a chemically simple system that saturates in rutile at ~20 mol% TiO_2 (two orders of magnitude greater than rhyolite melts), and future experimental work on more natural compositions should be performed to determine whether similar over- or underestimation via $a_{TiO_2}^{rut\text{-}sat}$ is observed in natural composition systems. This study lays the groundwork for calculating $a_{TiO_2}^{melt\text{-}sat}$ using multiple techniques in a single experiment (in this case, $a_{TiO_2}^{rut\text{-}sat}$ and $a_{TiO_2}^{Ti\text{-}in\text{-}tridymite}$) as a means to test the validity of assumptions that underlie trace-element thermobarometry. We strongly caution against using the data presented in this manuscript to interpret natural phenomena until experiments are performed on more natural bulk compositions.

In natural composition glasses (e.g., rhyolites), we were unable to use Raman to resolve potential changes in Ti coordination in melts as a function of bulk Ti content due to the low concentration of Ti and subsequently small signal relative to Si in the Raman spectra. Future work using Ti *K*-edge XANES (Farges 1997) could help resolve whether the same shifts in Ti solubility mechanisms—and subsequent deviations from Henrian behavior of Ti in melts—is observed in natural composition magmas.

It is difficult if not impossible to perform experiments in a reasonable time frame on quartz- and zircon-saturated rhyolitic magmas with crystals that are large enough to measure via EPMA. In light of this, experiments on simple systems like those performed in the present study can provide insight into the potential behavior of silicic magmas. Despite the limitations of applying Na-silicate composition experiments directly to natural systems, it is prudent to consider how observations like those made in this study could potentially affect observations of natural systems. In particular, we will consider the application to trace-element thermobarometry.

Although there is limited data available on coordination of Ti in natural composition glasses, the data available suggests there are large composition-dependent differences in Ti coordination for differing glass compositions. For example, Farges and Brown (1997) demonstrated that basaltic composition glasses incorporated Ti in various mixtures of $^{[5]}$Ti and $^{[6]}$Ti, whereas rhyolites incorporate Ti in varying proportions of $^{[4]}$Ti and $^{[5]}$Ti. For a given composition, Ti coordination has also been suggested to be a function of temperature (Lange and Navrotsky 1993). All of these observations are indirectly supported by differences in Ti solubility in glasses as a function of composition (Hayden and Watson 2007; Gaetani et al. 2008; Kularatne and Audétat 2014), including a strong increase in Ti solubility in Si-rich peralkaline relative to peraluminous glasses (Kularatne and Audétat 2014). All of these factors indicate that Ti solubility in melts and glasses is sensitive to composition and temperature and is incorporated by multiple substitution mechanisms. The most likely outcome of multiple solubility mechanisms is a change in the $\gamma_{TiO_2}^{melt}$ as a function of $X_{TiO_2}^{melt}$, which could affect Ti activity estimates utilizing rutile-saturation models.

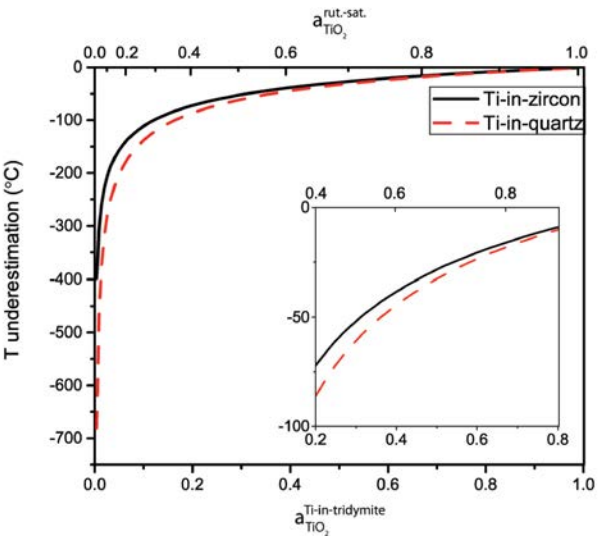

Figure 10. Application of the second-order polynomial fit to the experimental data from this study (Eq. 5) to rutile-saturation underestimation of $a_{TiO_2}^{melt\text{-}sat}$ for Ti-in-quartz and Ti-in-zircon thermobarometry. If natural magmas behave in a non-Henrian manner as observed in our experiments, rutile-saturation estimates of $a_{TiO_2}^{melt\text{-}sat}$ will underestimate crystallization temperatures. Given that the amount of Ti required to saturate our experiments in Ti is significantly greater than Ti saturation concentrations in many natural silicic magmas, the effects observed here are likely a worst-case scenario for rutile-saturation model estimates. (Color online.)

If the results of our study are extended to applications of trace-element thermobarometry, the potential effects of Ti on temperature estimates are significant. Non-Henrian behavior of Ti in melts in equilibrium with quartz and zircon would result in underestimation of temperatures that rely solely on rutile-saturation activity models (Fig. 10). These underestimations should not be applied directly to natural systems but provide an indication of the potential implications of multiple Ti-solubility mechanisms on Ti activity estimates. Given the amount of Ti required to saturate our experiments in TiO_2, the estimates shown in Figure 10 are likely a worst-case scenario for rutile-saturation estimates. When possible, applications of Ti-based trace element thermobarometry should be undertaken with multiple estimates of Ti activity and with care when assessing equilibrium for both melt compositions and mineral-mineral pairs utilized to determine $a_{TiO_2}^{melt\text{-}sat}$.

Acknowledgments and Funding

We thank the editorial staff, Calvin Miller, and one anonymous reviewer for comments that aided in the clarity and interpretation of the data presented within

this manuscript. We also thank Jeff Post for his assistance with XRD measurements. This work was funded by the Carnegie Postdoctoral Fellowship program.

References cited

Armstrong, J.T. (2014) Comparative performance of SDD-EDS and WDS detectors for quantitative analysis of mineral specimens: The next generation electron microprobe. Microscopy and Microanalysis, 20, 692–693.

Bell, R.J., Bird, N.F., and Dean, P. (1968) The vibrational spectra of vitreous silica, germania and beryllium fluoride. Journal of Physics C: Solid State Physics, 1, 299.

Chandrasekhar, H.R., Chandrasekhar, M., and Manghnani, M.H. (1980) Phonons in TiO_2–SiO_2 glasses. Journal of Non-Crystalline Solids, 40, 567–575.

Cody, G.D., Mysen, B.O., and Lee, S.K. (2005) Structure vs. composition: A solid state ^{1}H and ^{29}Si NMR study of quenched glasses along the Na_2O-SiO_2-H_2O join. Geochimica et Cosmochimica Acta, 69, 2373–2384.

Farges, F. (1997) Coordination of Ti^{4+} in silicate glasses: A high-resolution XANES spectroscopy study at the Ti K edge. American Mineralogist, 82, 36–43.

Farges, F., and Brown, G.E. (1997) Coordination chemistry of titanium (IV) in silicate glasses and melts: IV. XANES studies of synthetic and natural volcanic glasses and tektites at ambient temperature and pressure. Geochimica et Cosmochimica Acta, 61, 1863–1870.

Ferry, J.M., and Watson, E.B. (2007) New thermodynamic models and revised calibrations for the Ti-in-zircon and Zr-in-rutile thermometers. Contributions to Mineralogy and Petrology, 154, 429–437.

Gaetani, G.A., Asimow, P.D., and Stolper, E.M. (2008) A model for rutile saturation in silicate melts with applications to eclogite partial melting in subduction zones and mantle plumes. Earth and Planetary Science Letters, 272, 720–729.

Ghiorso, M.S., and Gualda, G.A.R. (2013) A method for estimating the activity of titania in magmatic liquids from the compositions of coexisting rhombohedral and cubic iron–titanium oxides. Contributions to Mineralogy and Petrology, 165, 73–81.

Glasser, F.P., and Maar, J. (1979) Phase relations in the system Na_2O-TiO_2-SiO_2. Journal of the American Ceramic Society, 62, 42–47.

Hayden, L.A., and Watson, E.B. (2007) Rutile saturation in hydrous siliceous melts and its bearing on Ti-thermometry of quartz and zircon. Earth and Planetary Science Letters, 258, 561–568.

Henderson, G.S., and Fleet, M.E. (1995) The structure of Ti-silicate glasses by microRaman spectrocopy. Canadian Mineralogist, 33, 399–408.

Henderson, G.S., Liu, X., and Fleet, M.E. (2002) A Ti L-edge X-ray absorption study of Ti-silicate glasses. Physics and Chemistry of Minerals, 29, 32–42.

Hofmann, A.E., Baker, M.B., and Eiler, J.M. (2013) An experimental study of Ti and Zr partitioning among zircon, rutile, and granitic melt. Contributions to Mineralogy and Petrology, 166, 235–253.

Huang, R., and Audétat, A. (2012) The titanium-in-quartz (TitaniQ) thermobarometer: A critical examination and re-calibration. Geochimica et Cosmochimica Acta, 84, 75–89.

Johannes, W. (1984) Beginning of melting in the granite system Qz-Or-Ab-An-H_2O. Contributions to Mineralogy and Petrology, 86, 264–273.

Kularatne, K., and Audétat, A. (2014) Rutile solubility in hydrous rhyolite melts at 750–900°C and 2kbar, with application to titanium-in-quartz (TitaniQ) thermobarometry. Geochimica et Cosmochimica Acta, 125, 196–209.

Lange, R.A., and Navrotsky, A. (1993) Heat capacities of TiO_2-bearing silicate liquids: Evidence for anomalous changes in configurational entropy with temperature. Geochimica et Cosmochimica Acta, 57, 3001–3011.

Le Losq, C., Mysen, B.O., and Cody, G.D. (2015) Water and magmas: insights about the water solution mechanisms in alkali silicate melts from infrared, Raman, and ^{29}Si solid-state NMR spectroscopies. Progress in Earth and Planetary Science, 2.

Maaløe, S., and Wyllie, P.J. (1975) Water content of a granite magma deduced from the sequence of crystallization determined experimentally with water-undersaturated conditions. Contributions to Mineralogy and Petrology, 52, 175–191.

McMillan, P. (1984) Structural studies of silicate glasses and melts—applications and limitations of Raman spectroscopy. American Mineralogist, 69, 622–644.

McMillan, P., Piriou, B., and Couty, R. (1984) A Raman-study of pressure-densified vitreous silica. Journal of Chemical Physics, 81, 4234–4236.

Mysen, B.O. (2011) Amorphous Materials: An experimental study of phosphorous and aluminosilicate speciation in and partitioning between aqueous fluids and silicate melts determined in-situ at high temperature and pressure. American Mineralogist, 96, 1636–1649.

Mysen, B., and Neuville, D. (1995) Effect of temperature and TiO_2 content on the structure of $Na_2Si_2O_5$–$Na_2Ti_2O_5$ melts and glasses. Geochimica et Cosmochimica Acta, 59, 325–342.

Mysen, B.O., and Richet, P. (2005) Silicate Glasses and Melts: Properties and Structure. Elsevier.

Piwinskii, A.J. (1973) Experimental studies of granitoids from the Central and Southern Coast Ranges, California. Tschermaks mineralogische und petrographische Mitteilungen, 20, 107–130.

Reynard, B., and Webb, S.L. (1998) High-temperature Raman spectroscopy of $Na_2TiSi_2O_7$ glass and melt: coordination of Ti^{4+} and nature of the configurational changes in the liquid. European Journal of Mineralogy, 10, 49–58.

Roskosz, M., Mysen, B.O., and Cody, G.D. (2006) Dual speciation of nitrogen in silicate melts at high pressure and temperature: An experimental study. Geochimica et Cosmochimica Acta, 70, 2902–2918.

Ryerson, F.J. (1985) Oxide solution mechanisms in silicate melts: Systematic variations in the activity coefficient of SiO_2. Geochimica et Cosmochimica Acta, 49, 637–649.

Scannell, G., Barra, S., and Huang, L. (2016) Structure and properties of Na_2O-TiO_2-SiO_2 glasses: Role of Na and Ti on modifying the silica network. Journal of Non-Crystalline Solids, 448, 52–61.

Seifert, F., Mysen, B., and Virgo, D. (1983) Raman-study of densified vitreous silica. Physics and Chemistry of Glasses, 24, 141–145.

Sen, P.N., and Thorpe, M.F. (1977) Phonons in AX2 glasses: From molecular to band-like modes. Physical Review B, 15, 4030–4038.

Shane, P., Smith, V.C., and Nairn, I. (2008) Millennial timescale resolution of rhyolite magma recharge at Tarawera volcano: insights from quartz chemistry and melt inclusions. Contributions to Mineralogy and Petrology, 156, 397–411.

Thomas, J.B., and Watson, E.B. (2012) Application of the Ti-in-quartz thermobarometer to rutile-free systems. Reply to: a comment on: 'TitaniQ under pressure: the effect of pressure and temperature on the solubility of Ti in quartz' by Thomas et al. Contributions to Mineralogy and Petrology, 164, 369–374.

Thomas, J.B., Watson, E.B., Spear, F.S., Shemella, P.T., Nayak, S.K., and Lanzirotti, A. (2010) TitaniQ under pressure: the effect of pressure and temperature on the solubility of Ti in quartz. Contributions to Mineralogy and Petrology, 160, 743–759.

Wark, D.A., and Watson, E.B. (2006) TitaniQ: a titanium-in-quartz geothermometer. Contributions to Mineralogy and Petrology, 152, 743–754.

Wark, D.A., Hildreth, W., Spear, F.S., Cherniak, D.J., and Watson, E.B. (2007) Pre-eruption recharge of the Bishop magma system. Geology, 35, 235–238.

Watson, E.B., and Harrison, T.M. (2005) Zircon thermometer reveals minimum melting conditions on earliest Earth. Science, 308, 841–844.

Zotov, N., and Keppler, H. (1998) The influence of water on the structure of hydrous sodium tetrasilicate glasses. American Mineralogist, 83, 823–834.

Manuscript received December 2, 2019
Manuscript accepted March 16, 2020
Manuscript handled by Daniel Neuville

Endnote:

[1]Deposit item AM-20-107391, Supplementary Material. Deposit items are free to all readers and found on the MSA website, via the specific issue's Table of Contents (go to http://www.minsocam.org/MSA/AmMin/TOC/2020/Oct2020_data/Oct2020_data.html).